Reaction Kinetics, Mechanisms and Catalysis (2022) 135:2533–2550
https://doi.org/10.1007/s11144-022-02276-w

Selective hydrogenation of phenylacetylene over non-precious bimetallic Ni–Zn/SiO_2 and Ni–Co/SiO_2 catalysts prepared by glucose pyrolysis

Wei Chen[1] · Zhichang Bao[1] · Zhiming Zhou[1]

Received: 16 May 2022 / Accepted: 28 July 2022 / Published online: 2 August 2022

Abstract

A series of non-precious bimetallic NiM_x/SiO_2 (M = Zn or Co) catalysts with a fixed Ni loading of 5 wt% and different molar ratios of M/Ni (0.004–1.97) were prepared by glucose pyrolysis and applied to the selective hydrogenation of phenylacetylene. The properties of the catalysts were characterized by N_2 physisorption, CO chemisorption, ICP-OES, TGA, XRD, HRTEM, XPS, and DRIFTS. The activity and selectivity of the bimetallic catalysts could be tuned by varying the Zn/Ni and Co/Ni molar ratios, which were almost independent of the metal particle size (with a similar size of 4.1–5.5 nm), but predominantly determined by the geometric and/or electronic effects of the catalysts. Among all the catalysts studied, $NiZn_{0.05}/SiO_2$ and $NiCo_{0.09}/SiO_2$ presented higher selectivity to styrene (86.3% and 88.0%, respectively) at above 99% conversion of phenylacetylene. The high selectivity of the former was attributed to the geometric and electronic effects of the Ni–Zn alloy, while the latter was due to the geometric effect caused by the addition of Co. The activity and selectivity of $NiCo_{0.09}/SiO_2$ were maintained during six consecutive cycles, indicating its good stability in the selective hydrogenation of phenylacetylene.

Keywords Non-precious catalyst · Bimetallic catalyst · Selective hydrogenation · Phenylacetylene · Geometric and electronic effects

Introduction

Styrene is a very important precursor in the petrochemical industry and has been widely used for production of plastics and synthetic rubbers such as polystyrene, acrylonitrile–butadiene–styrene resins and styrene-butadiene rubber [1]. The global market value of styrene is expected to grow from $48.8 billion in 2020 to $69.9

✉ Zhiming Zhou
zmzhou@ecust.edu.cn

[1] School of Chemical Engineering, East China University of Science and Technology, Shanghai 200237, China

billion in 2027 [2]. Nowadays, the main processes of styrene production are ethylbenzene dehydrogenation, styrene-propylene oxide co-production, and extraction from pyrolysis gasoline (pygas, a by-product of steam cracking of naphtha) [3–5]. However, a small amount of phenylacetylene is always present in the styrene feedstock, which will poison downstream polymerization catalysts [6, 7]. The similar properties of phenylacetylene and styrene make it difficult to separate them by distillation. At present, selective hydrogenation of phenylacetylene is the most efficient method to remove phenylacetylene from styrene, with the aim of achieving complete conversion of phenylacetylene while avoiding over-hydrogenation of styrene as much as possible. The main challenge for this process is the development of effective catalysts with high selectivity and stability.

To date, noble metal Pd-based catalysts have been the dominant materials in the selective hydrogenation of alkynes because of their excellent hydrogenation activity [8, 9]. However, due to the strong adsorption ability of Pd active site for the intermediate product–styrene, styrene cannot be desorbed in time but is further hydrogenated to ethylbenzene. Therefore, the selectivity to styrene on monometallic Pd catalysts typically decreases rapidly as the reaction approaches complete conversion of phenylacetylene, resulting in loss of styrene [10–13]. Various methods have been developed to enhance the selectivity of Pd-based catalysts, including alloying Pd with relatively inert metals such as Cu [14, 15], Zn [15, 16] and Pb [17, 18], tuning metal-support interaction [10, 19], and confining Pd nanoparticles in porous materials [20, 21]. In fact, the commercial Lindlar catalyst used for this reaction is 5 wt% $Pd/CaCO_3$ modified with lead acetate or quinoline, which has environmental concerns and is also constrained by the scarcity and high cost of the precious metal Pd [22, 23].

Among non-precious metal alternatives, Ni-based catalysts are the most extensively studied due to their relatively high hydrogenation activity. In order to improve the selectivity to styrene over Ni-based catalysts, alloys/intermetallics are usually formed by combining Ni with another metal (Zn [24, 25], Cu [26], Ga [27, 28], and Sn [28]) or non-metal component (Si [29–31] and P [32, 33]) to optimize the geometric and electronic structure of the Ni active site. It is generally reported that the type and doping amount of the second metal have impacts on the particle size of metal nanoparticles, which, however, is not conducive to explore the effect of the second metal because the activity and selectivity of the catalyst in the selective hydrogenation of phenylacetylene is greatly influenced by the metal particle size [24, 27, 33]. Indeed, the conventional preparation of bimetallic alloy catalysts requires that the two metal precursors loaded on the support undergo a high-temperature reduction step in H_2 atmosphere, which inevitably leads to the agglomeration of metal nanoparticles [34, 35]. Although the liquid-phase reduction method can be used to prepare alloys, the process is often more complex and the choice of solvent, capping agent, and reducing agent needs to be carefully considered [28, 35]. Therefore, it is necessary to develop a facile synthetic strategy for alloy catalysts with uniform particle distribution and controllable composition.

In 2013, Beller's group [36] developed an efficient strategy for the preparation of catalysts by high-temperature pyrolysis of iron-phenanthroline complexes supported on carbon in an inert atmosphere. The resulting Fe-phen/C-800 catalyst

achieved good to excellent yields in selective hydrogenation of more than 80 diverse nitroarenes. Then, this strategy was extended to the preparation of Co- and Ni-based catalysts and applied to the hydrogenation of various unsaturated compounds including alkynes [37–40]. Recently, the same group [41] prepared monodisperse nickel nanoparticle catalysts by simple pyrolysis of monosaccharide-nickel acetate templates loaded on silica, which showed high selectivity in the stereo- and chemoselective hydrogenation of functionalized and structurally diverse alkynes. However, it remains unclear whether this strategy allows the preparation of highly dispersed Ni-based bimetallic alloy catalysts.

In this work, a series of bimetallic Ni–Zn/SiO_2 and Ni–Co/SiO_2 catalysts were prepared by pyrolysis of glucose and acetates supported on silica and applied to the selective hydrogenation of phenylacetylene to styrene. The effects of Zn/Ni and Co/Ni molar ratios on the structure and performance of the catalysts were investigated and the structure–activity/selectivity relationship was explored. Finally, the reusability of the best catalyst and the effect of reaction temperature and pressure on the catalytic performance were studied.

Experimental section

Materials

Nickel acetate tetrahydrate ($Ni(OAc)_2{\cdot}4H_2O, \geq 99\%$), zinc acetate ($Zn(OAc)_2, \geq 99\%$), cobalt acetate tetrahydrate ($Co(OAc)_2{\cdot}4H_2O, \geq 99\%$), D-glucose ($C_6H_{12}O_6, \geq 99\%$), *n*-octane ($C_8H_{18}, \geq 98\%$), and absolute ethanol ($C_2H_5OH, \geq 99.7\%$) were purchased from Adamas Reagent Co., Ltd., China. Phenylacetylene ($C_8H_6, > 98\%$) was obtained from Alfa Aesar. SiO_2 (Hydrophilic-380, particle size of 7–40 nm) was supplied by Makclin Biochemical Co., Ltd., China. All chemicals were used without treatment.

Catalyst preparation

Ni/SiO_2 catalyst was prepared by a modified pyrolysis technique [41]. First, 133.8 mg of $Ni(OAc)_2{\cdot}4H_2O$, 150 mg of D-glucose, 10 mL of deionized water, and 30 mL of ethanol were added into a 100 mL round-bottomed flask equipped with a reflux condenser. After stirring for 5 min at room temperature, the flask was immersed in a water bath at 60 °C and stirred for 2 h at 750 rpm. 0.6 g of SiO_2 was then added and stirred for another 2 h at the same temperature. Next, solvent was evaporated from the solution using a rotary evaporator at 60 °C until a light-green powder was obtained. The powder was further dried in an oven at 110 °C for 10 h. Finally, the powder was placed in a quartz tube and inserted into an electronic furnace. The powder was heated to 800 °C at a heating rate of 25 °C min^{-1} and held at 800 °C for 2 h under flowing N_2. The obtained black powder was Ni/SiO_2 with a nominal Ni loading of 5 wt%.

The Ni–Zn/SiO_2 and Ni–Co/SiO_2 bimetallic catalysts were prepared by the same method except that $Zn(OAc)_2$ or $Co(OAc)_2{\cdot}4H_2O$ was added together with $Ni(OAc)_2{\cdot}4H_2O$. The theoretical molar ratios of Zn/Ni or Co/Ni in the bimetallic catalysts were 0.1, 0.5, 1, and 2. However, the evaporation of Zn during pyrolysis resulted in quite low actual Zn/Ni molar ratios of 0.004, 0.02, 0.05, and 0.07, which were determined by inductively coupled plasma-optical emission spectroscopy. For clarity, the resulting catalysts were denoted by $NiZn_x/SiO_2$ or $NiCo_x/SiO_2$, where x represents the actual molar ratio of Zn/Ni or Co/Ni. Metal-free G/SiO_2 (pyrolysis of glucose supported on SiO_2) and monometallic Co/SiO_2 (nominal Co loading of 5 wt%) were prepared by the same method. In addition, Ni/SiO_2-I and ZnO/SiO_2-I (both Ni and Zn at 5 wt% nominal metal loading) were prepared by conventional impregnation: nickel acetate or zinc acetate was first impregnated on SiO_2, and then dried at 110 °C, followed by calcination at 500 °C. Ni/SiO_2-I was further reduced in 30% H_2/N_2 at 500 °C.

Catalyst characterization

The Brunauer–Emmett–Teller (BET) surface area, pore volume (V_p), and average pore diameter (d_p) of samples were acquired from N_2 adsorption–desorption isotherms at − 196 °C using a Micrometrics ASAP 2010 instrument. The crystalline structure of catalyst was characterized by X-ray diffraction (XRD, Rigaku D/Max 2550 VB/PC) using Cu Kα radiation ($\lambda = 0.15406$ nm) in the range of $2\theta = 10°–80°$ with a step size of 0.02°. The micro-morphology of catalyst was observed by high-resolution transmission electron microscopy (HRTEM, JEOL JEM-2100). The average metal particle size was obtained by measuring at least 100 particles. The surface composition of catalyst was analyzed by X-ray photoelectron spectroscopy (XPS, Thermo Scientific ESCALAB 250 Xi) using the Al Kα radiation ($h\nu = 1486.6$ eV) and a pass energy of 40 eV, with the binding energy referenced by C 1s (284.8 eV). The amount of active sites of catalyst was determined by CO-pulse chemisorption (Micromeritics AutoChem 2920), assuming the chemisorption stoichiometry of CO/Ni = 1. Before measurements, the catalyst was reduced at 300 °C for 1 h in 10% H_2/Ar, followed by switching to He at 330 °C for 30 min to remove adsorbed H_2. After the catalyst was cooled to room temperature in He, CO pulses were injected until the CO peak area remained constant, and the CO uptake was monitored by a thermal conductivity detector. The metal loading of catalyst was measured by inductively coupled plasma-optical emission spectroscopy (ICP-OES, Varian 710-ES). The weight loss of samples before and after pyrolysis was quantified by thermogravimetric analysis (TGA, PerkinElmer TGA-4000) heated from room temperature to 800 °C at 10 °C min^{-1} in N_2 and air flow. The content and structure of carbon in the catalyst were examined by elemental analyzer (Elementar VARIO ELIII) and Raman spectroscopy (Renishaw inVia Reflex, 514 nm excitation wavelength). The structural properties of Ni active sites in the catalyst were probed by diffuse reflectance infrared Fourier transform spectroscopy (DRIFTS, Bruker Tensor 27) after chemisorption of CO. The catalyst was first pretreated at 300 °C for 1 h in 10% H_2/Ar, then cooled to room temperature under Ar flow and the background spectrum

was recorded. Afterwards, 5% CO/Ar was passed through for 30 min to saturate the surface, followed by purging with Ar for 10 min to remove gaseous and weakly adsorbed CO, and the spectrum was collected by 32 scans at a resolution of 4 cm^{-1}.

Catalyst test

The selective hydrogenation of phenylacetylene over various catalysts was performed in a semi-batch stirred tank reactor (300 mL, Parr 5100). Typically, 0.15 g of catalyst powder, 5 g of phenylacetylene, 5 g of *n*-octane (internal standard), and 90 g of ethanol (solvent) were first added into the reactor and heated to 60 °C in N_2. Then, H_2 was charged into the reactor to purge N_2 for five times. Finally, the hydrogenation reaction started at 60 °C and 0.5 MPa in H_2 with vigorously stirring at 1000 rpm. About 1 mL of liquid phase was discharged from the reactor in a certain interval and analyzed using a gas chromatography (Hewlett-Packard 6890) equipped with a capillary column (PEG-20M, 30 m × 0.32 mm × 0.50 μm) and a flame ionization detector.

The conversion of phenylacetylene and the selectivity to styrene are defined as follows:

$$\text{Conversion} = \frac{\text{Moles of phenylacetylene converted}}{\text{Moles of initial phenylacetylene}} \times 100\% \quad (1)$$

$$\text{Selectivity} = \frac{\text{Moles of styrene produced}}{\text{Moles of phenylacetylene converted}} \times 100\% \quad (2)$$

The catalyst activity is expressed in terms of the initial rate (R_{ini}) that is defined as the number of moles of phenylacetylene consumed per second per gram of catalyst during the initial period. The R_{ini} is calculated by:

$$R_{ini} = \frac{F\alpha}{tm} \quad (3)$$

Here F is the number of moles of phenylacetylene in the feedstock, mol; α is the conversion of phenylacetylene; t is the reaction time, s; m is the mass of catalyst, g. The conversion data used to calculate R_{ini} is below 30%.

Results and discussion

Physicochemical properties of catalysts

Fig. S1a shows the TGA curves of glucose, $Ni(OAc)_2{\cdot}4H_2O$, and the precursors (without calcination treatment) of Ni/SiO_2, $NiZn_{0.05}/SiO_2$ and $NiCo_{1.02}/SiO_2$ in N_2 flow. For glucose, a weight loss of around 78% occurs between 180 and 420 °C, which is assigned to the pyrolysis of glucose [42]. For $Ni(OAc)_2{\cdot}4H_2O$, two distinct weight loss steps are observed. The weight loss (28.7%) below 120 °C is

caused by the removal of crystal water (the weight percentage of crystal water in $Ni(OAc)_2{\cdot}4H_2O$ is 28.9%), while the weight loss (33.2%) in the temperature range of 250 to 420 °C is due to the decomposition of $Ni(OAc)_2$. The precursors of Ni/SiO_2, $NiZn_{0.05}/SiO_2$, and $NiCo_{1.02}/SiO_2$ exhibit similar TGA curves with a weight loss of about 30% below 500 °C, which is mainly attributed to the decomposition of acetates and glucose. The pyrolysis of glucose in N_2 atmosphere can yield reductive agents such as C and CO [43], which in turn can reduce nickel oxides (derived from decomposition of nickel acetate) immediately.

After pyrolysis treatment, Ni/SiO_2, $NiZn_{0.05}/SiO_2$, and $NiCo_{1.02}/SiO_2$ are further characterized by TGA in air. As presented in Fig. S1b, the initial weight loss below 130 °C is due to desorption of physisorbed water. After then, a weight gain at 130–320 °C takes place for all the three catalysts, which is attributed to the oxidation of metals. The weight gain of Ni/SiO_2 is quite similar to that of $NiZn_{0.05}/SiO_2$, but distinctly lower than that of $NiCo_{1.02}/SiO_2$. This is because: (1) the actual amount of Zn in $NiZn_{0.05}/SiO_2$ is very low (0.3 wt%, Table 1), and the possible contribution from Zn oxidation to the weight gain can be neglected; (2) the actual amount of Co in $NiCo_{1.02}/SiO_2$ is comparable to that of Ni (4.9 wt%, Table 1), and the metallic Co derived from the pyrolysis step is also oxidized, which contributes to the weight gain. For other $NiZn_x/SiO_2$ catalysts, the actual Zn content is also much lower than the nominal content (Table 1), which is ascribed to evaporation of zinc during the pyrolysis process at high temperatures [20, 44]. It is known that the boiling point of Ni, Co, and Zn is 2732, 2870, and 907 °C. Therefore, the metallic Ni and Co remain in the catalysts, which justifies the similarity between nominal and actual Co/Ni molar ratios in the catalysts (Table 1). After this weigh gain, a weight loss is observed for all samples, owing to the gasification of carbon. Indeed, the elemental analysis shows that the carbon content in Ni/SiO_2 is 5.3 wt%, and the presence of layered carbon is also confirmed by Raman spectroscopy (Fig. S2). However, another weight gain appears on $NiCo_{1.02}/SiO_2$ at above 650 °C, which corresponds to the $CoO \rightarrow Co_3O_4$ process [45].

Fig. S3 shows the XRD patterns of $NiZn_x/SiO_2$ and $NiCo_x/SiO_2$ catalysts, and the corresponding local enlargements are given in Fig. 1. The broad peak located at $2\theta = 15°–35°$ for all samples belongs to amorphous SiO_2. Ni/SiO_2 exhibits diffraction peaks at $2\theta = 44.5°$ and 51.8° (Fig. S3a), corresponding to metallic Ni(111) and Ni(200) planes (JCPDS 04-0850). Co/SiO_2 shows diffraction peaks at $2\theta = 44.2°$ and 51.5° (Fig. S3b) that are indexed to metallic Co(111) and Co(200), respectively (JCPDS 15-0806). The presence of metallic Ni and Co peaks further demonstrates the reduction of nickel and cobalt oxides during pyrolysis of glucose in N_2. For $NiZn_x/SiO_2$ (Fig. 1a), with increasing the Zn/Ni molar ratio, the Ni(111) peak first shifts to a lower angle and then recovers to 44.5° when the Zn/Ni ratio is 0.07, implying the formation of Ni–Zn alloy on some $NiZn_x/SiO_2$ [46, 47]. Similarly, with increasing the Co/Ni molar ratio, this peak shifts to a lower angle between 44.5° (Ni(111) plane) and 44.2° (Co(111) plane), suggesting the formation of Ni–Co alloy [48, 49].

Fig. S4 displays the N_2 adsorption–desorption isotherms and the pore size distribution curves of SiO_2, $NiZn_x/SiO_2$, and $NiCo_x/SiO_2$. All catalysts exhibit type IV isotherms with H3-type hysteresis loops [50], indicating that the mesoporous

Table 1 Physicochemical properties of support and catalysts

Sample	Metal loading[a]		S_{BET} ($m^2\ g^{-1}$)	V_p[b] ($cm^3\ g^{-1}$)	d_p[b] (nm)	CO uptake (μmol g^{-1})	d_{metal}[c] (nm)	R_{ini}[d] (μmol/(g s))
	(Ni | M) (wt%)	M/Ni ratio						
SiO_2	–	–	359.2	0.94	13.9	–	–	–
Ni/SiO_2	5.1	–	306.3	1.05	16.1	3.69	3.8 ± 1.2	16.32
$NiZn_{0.004}/SiO_2$	5.1 | 0.02	0.004	304.9	1.19	17.7	2.68	4.2 ± 1.1	11.60
$NiZn_{0.02}/SiO_2$	4.9 | 0.1	0.02	303.0	0.89	13.6	1.25	4.8 ± 1.5	6.12
$NiZn_{0.05}/SiO_2$	5.2 | 0.3	0.05	299.8	0.97	15.0	0.89	5.0 ± 1.5	4.48
$NiZn_{0.07}/SiO_2$	4.9 | 0.4	0.07	256.9	0.96	15.6	1.85	5.5 ± 1.3	8.07
$NiCo_{0.09}/SiO_2$	5.3 | 0.5	0.09	298.7	0.88	13.7	0.67	4.1 ± 1.1	3.02
$NiCo_{0.52}/SiO_2$	5.0 | 2.6	0.52	288.1	0.93	14.6	0.92	4.2 ± 1.0	4.56
$NiCo_{1.02}/SiO_2$	4.8 | 4.9	1.02	270.3	0.83	13.8	0.72	4.5 ± 1.4	4.15
$NiCo_{1.97}/SiO_2$	5.2 | 10.3	1.97	247.0	0.53	9.3	0.53	5.3 ± 1.4	2.51
Co/SiO_2	4.9	–	261.1	0.85	14.7	0.43	7.7 ± 2.0	1.72

[a]Determined by ICP-OES

[b]Acquired from the desorption branch of the N_2 isotherm by the BJH method

[c]Average metal particle size is obtained by HRTEM

[d]Calculated using the conversion data below 30%

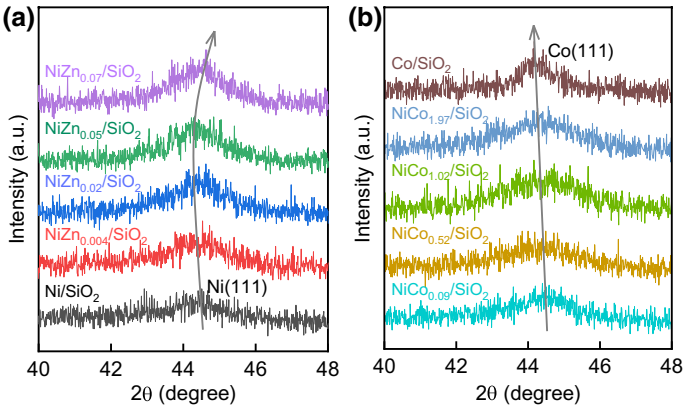

Fig. 1 Local enlarged XRD patterns of **a** $NiZn_x/SiO_2$ and **b** $NiCo_x/SiO_2$

structure of SiO_2 is maintained after introduction of Ni and Zn or Co. In addition, all catalysts except $NiCo_{1.97}/SiO_2$ have a unimodal pore size distribution centered at around 20 nm, whereas $NiCo_{1.97}/SiO_2$ shows a bimodal pore size distribution (about 6 and 20 nm diameter pores). The specific surface area of all catalysts is reduced as compared to the support (Table 1) due to the metal deposition, while the pore volume and average pore size of the catalysts (excluding $NiCo_{1.97}/SiO_2$) have a small variation. For $NiCo_{1.97}/SiO_2$, the total metal loading (15.5 wt%) is much higher than that of other catalysts (5–9.7 wt%), so that more pores of $NiCo_{1.97}/SiO_2$ are blocked, leading to a bimodal pore size distribution and a decreased pore volume.

Fig. S5 shows the HRTEM images and the metal particle size distribution of $NiZn_x/SiO_2$ and $NiCo_x/SiO_2$. The metal particles are uniformly distributed over all catalysts with a narrow particle size distribution. The average metal particle sizes of Ni/SiO_2 and Co/SiO_2 are 3.8 and 7.7 nm, respectively. By contrast, the average metal particle sizes of bimetallic catalysts increase slightly with increasing the Zn/Ni or Co/Ni ratio, varying from 4.2 to 5.5 nm for $NiZn_x/SiO_2$ or from 4.1 to 5.3 nm for $NiCo_x/SiO_2$ (Table 1). Apparently, both Ni–Zn and Ni–Co bimetallic catalysts have similar metal particle sizes irrespective of variation in composition, so the effect of metal particle size on the catalytic performance can be ignored in the following discussion. Ni/SiO_2 displays lattice spacings of 0.203 and 0.176 nm (determined by fast Fourier transform pattern (FFT)), corresponding to the (111) and (200) planes of *fcc* Ni. For $NiZn_{0.02}/SiO_2$ and $NiZn_{0.05}/SiO_2$, a larger lattice spacing of 0.206 nm is found (Fig. S5a), indicating the formation of Ni–Zn alloy by doping Zn atoms into the lattice of Ni [47, 51]. With further increasing the Zn/Ni ratio, a lattice spacing of 0.214 nm assigned to the ZnO(200) plane (JCPDS 65-0682) is observed on $NiZn_{0.07}/SiO_2$. As for $NiCo_x/SiO_2$ (Fig. S5b), a lattice spacing of 0.204 nm (between 0.203 nm of the Ni(111) plane and 0.205 nm of Co(111)) occurs in $NiCo_{0.52}/SiO_2$, $NiCo_{1.02}/SiO_2$, and $NiCo_{1.97}/SiO_2$, which results from an expansion of Ni lattice and implies the formation of Ni–Co alloy [48, 52]. For $NiCo_{1.97}/SiO_2$ with a high Co/Ni ratio of 1.97, another lattice spacing of 0.205 nm is identified, implying that not all Co particles are alloyed with Ni. The above results illustrate that the Ni–Zn (or

Ni–Co) alloy is formed in some bimetallic $NiZn_x/SiO_2$ (or $NiCo_x/SiO_2$), in accordance with the XRD analysis.

Fig. 2 presents the XPS spectra of Ni 2p core level of $NiZn_x/SiO_2$ and $NiCo_x/SiO_2$. For Ni/SiO_2 (Fig. 2a), the Ni $2p_{3/2}$ spectrum can be deconvoluted into three peaks with binding energies at 852.7, 856.2, and 860.1 eV, which are assigned to Ni^0, Ni^{2+}, and satellite peak [53, 54]. With the incorporation of Zn, the peak of Ni^0 shifts to 852.5 eV in $NiZn_{0.02}/SiO_2$ and further to 852.2 eV in $NiZn_{0.05}/SiO_2$ (Fig. 2a). According to the literature [47, 53], this implies electron transfer from Zn to Ni and the presence of electronic effect, although attempts to deconvolute the XPS spectrum of the Zn 2p core level fail because of the low Zn content (Fig. S6a). Note that the peak of Ni^0 in $NiZn_{0.004}/SiO_2$ and $NiZn_{0.07}/SiO_2$ remains at 852.7 eV, indicative of no electron transfer between Ni and Zn, which may be due to the very low Zn content and the presence of ZnO. As for bimetallic $NiCo_x/SiO_2$ (Fig. 2b), the Ni^0 $2p_{3/2}$ peak is located at 852.7 eV when x = 0.09, but with increasing x from 0.52 to 1.97, this peak gradually shifts positively from 852.9 to 853.7 eV; meanwhile, the Co^0 $2p_{3/2}$ peak varies between 778.0 and 778.8 eV (Fig. S6b), lower than that for Co/SiO_2 (779.0 eV). This reveals the electron transfer from Ni to Co [52, 55]. The finding from the XPS analysis is consistent with the XRD and HRTEM results. In short, the Ni–Zn alloy is formed in $NiZn_x/SiO_2$ (x = 0.02 and 0.05) where Ni atoms are electron-rich, while the Ni–Co alloy is present in $NiCo_x/SiO_2$ (x = 0.52, 1.02, and 1.97) where Ni atoms are electron-poor.

DRIFTS of CO chemisorption is used to further probe the structural information of Ni in the catalyst. Ni/SiO_2 is compared with Ni/SiO_2-I (prepared by conventional impregnation), and $NiCo_{1.02}/SiO_2$ is chosen as a representative bimetallic catalyst, considering the high content of the second metal. DRIFTS of CO adsorbed on Ni/SiO_2-I shows bands in the range of 2100–2000, 2000–1900, and 1900–1800 cm^{-1}

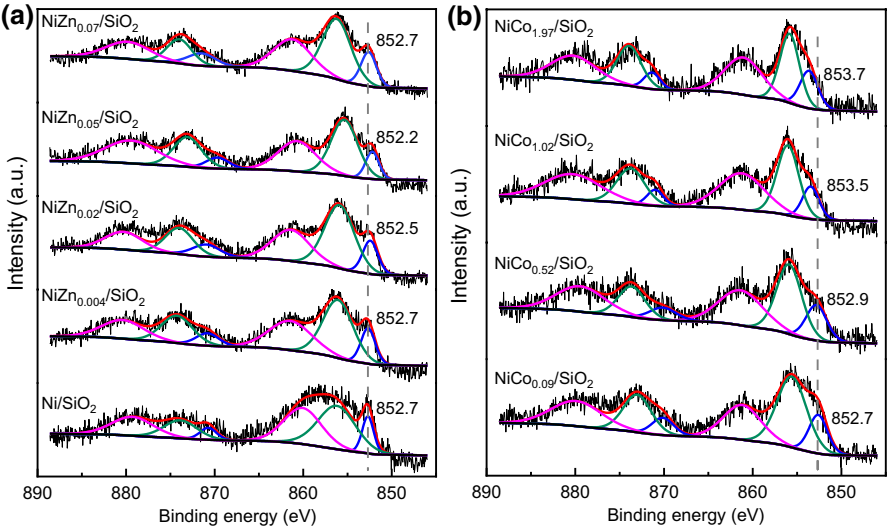

Fig. 2 XPS spectra of Ni 2p for **a** $NiZn_x/SiO_2$ and **b** $NiCo_x/SiO_2$ catalysts

(Fig. S7), which correspond to linearly, bridged, and multibonded adsorbed CO on Ni [56, 57]. Obviously, the bridged and multibonded adsorption peaks on Ni/SiO_2 almost disappear, while the linear adsorption peak at 2042 cm^{-1} with a shoulder at 2003 cm^{-1} is retained. This result can be attributed to the presence of carbon covering the surface of Ni nanoparticles, which hinders the formation of bridged and multibonded CO species with higher adsorption strength [56, 58]. For $NiCo_{1.02}/SiO_2$, only a peak of linearly adsorbed CO on Ni is observed located at 2052 cm^{-1}, considering no peaks of adsorbed CO on Co at room temperature [59, 60]. However, this peak is blue-shifted compared to Ni/SiO_2 because the electron-poor Ni decreases the electron back-donation from the d orbital of Ni to the $2\pi^*$ antibonding orbital of CO. The result of DRIFTS further confirms the XPS analysis that the electron transfer from Ni to Co occurs on $NiCo_{1.02}/SiO_2$. It should be noted that the absence of peaks below 2000 cm^{-1} on $NiCo_{1.02}/SiO_2$ cannot be explained as a geometric effect caused by Co doping, due to the interference of carbon in the catalyst. Therefore, CO-pulse chemisorption is carried out to further investigate the change in the number of active sites induced by the second metal doping.

The CO uptake data of various catalysts are summarized in Table 1. Ni/SiO_2 has the largest CO uptake (3.69 μmol g^{-1}) among all catalysts. After introducing Zn or Co, the CO uptake of bimetallic catalysts decreases without exception, owing to the dilution of the active phase [61, 62]. In general, bimetallic $NiZn_x/SiO_2$ catalysts have higher CO uptake than $NiCo_x/SiO_2$, which is associated with the much lower content of Zn that leads to a weak modification of Ni by Zn. For $NiZn_x/SiO_2$, the CO uptake gradually decreases with x from 0.004 to 0.05, but increases at $x = 0.07$. This is probably due to no Ni–Zn alloy formation on $NiZn_{0.07}/SiO_2$. With regard to bimetallic $NiCo_x/SiO_2$, $NiCo_{0.52}/SiO_2$ and $NiCo_{1.02}/SiO_2$ show higher CO uptake than $NiCo_{0.09}/SiO_2$, despite the fact that the latter has the lowest Co/Ni ratio and contains no Ni–Co alloy. This is probably because metallic Co is able to chemisorb CO, as evidenced by a CO uptake of 0.43 μmol g^{-1} on Co/SiO_2.

Activity and selectivity of catalysts

Fig. 3 compares the apparent activity and selectivity of different catalysts in the hydrogenation of phenylacetylene. Ni/SiO_2 shows the highest apparent activity in terms of the reaction time that is needed for complete conversion of phenylacetylene (conversion > 99%), while Co/SiO_2 has the lowest apparent activity. Bimetallic $NiZn_x/SiO_2$ (Fig. 3a) and $NiCo_x/SiO_2$ (Fig. 3c) rank between Ni/SiO_2 and Co/SiO_2 with regard to the apparent activity. Besides, G/SiO_2 (metal-free) and ZnO/SiO_2-I have no obvious hydrogenation activity due to the absence of active metals (Fig. S8), reflecting that the SiO_2 support and ZnO are almost inactive for phenylacetylene hydrogenation. The initial rates for each catalyst are calculated and listed in Table 1. It is found that the initial rates of either $NiZn_x/SiO_2$ or $NiCo_x/SiO_2$ are correlated positively with the CO uptake data, which is reasonable as the CO uptake reflects the number of active sites. The CO uptake and reaction rates of $NiCo_x/SiO_2$ are generally lower than those of $NiZn_x/SiO_2$, again confirming a

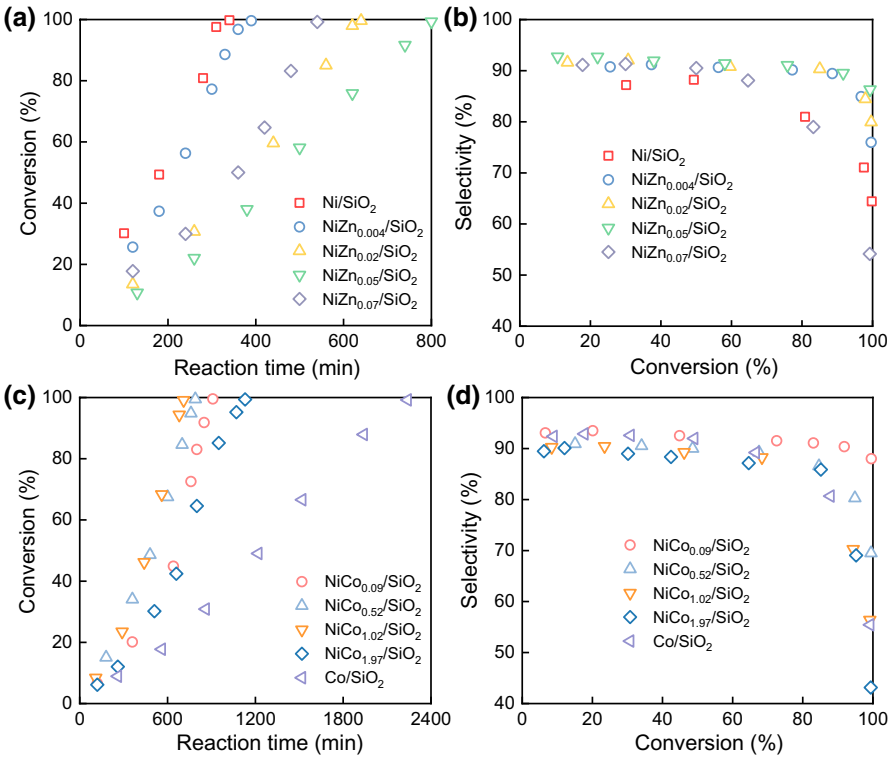

Fig. 3 **a**, **c** Conversion vs time and **b**, **d** selectivity vs conversion over $NiZn_x/SiO_2$ and $NiCo_x/SiO_2$ bimetallic catalysts (reaction condition: 60 °C, 0.5 MPa, 5 wt% phenylacetylene in ethanol, 0.15 g of catalyst, and 100 g of solution in a semi-batch stirred tank reactor)

weaker modification by Zn when compared to Co, which is owing to the low Zn content in $NiZn_x/SiO_2$ originating from the evaporation of Zn during pyrolysis.

The selectivity to styrene at complete conversion of phenylacetylene is of interest, which is an important indicator to evaluate the performance of the catalyst when considering the purpose of removing phenylacetylene from styrene. A high selectivity means that the loss of styrene caused by excessive hydrogenation in the removal of phenylacetylene can be avoided to a great extent. For $NiZn_x/SiO_2$, the selectivity to styrene at complete conversion of phenylacetylene follows the order $NiZn_{0.05}/SiO_2$ (selectivity: 86.3%) > $NiZn_{0.02}/SiO_2$ (79.9%) > $NiZn_{0.004}/SiO_2$ (76.0%) > Ni/SiO_2 (64.4%) > $NiZn_{0.07}/SiO_2$ (54.1%) (Fig. 3b). Except for $NiZn_{0.07}/SiO_2$, the selectivity of bimetallic $NiZn_x/SiO_2$ is greatly increased as compared to Ni/SiO_2. The improved selectivity of $NiZn_{0.05}/SiO_2$ and $NiZn_{0.02}/SiO_2$ can be attributed to both geometric and electronic effects induced by the formation of Ni–Zn alloy: on the one hand, the geometric effect reduces the number of active sites (as evidenced by the decreased CO uptake), whereby further hydrogenation of styrene to ethylbenzene can be inhibited to some extent [27, 28, 31]; on the other hand, the electron-rich Ni active sites can facilitate the desorption

of electron-rich styrene [24, 27, 28], resulting in an increased selectivity. The relatively high selectivity of $NiZn_{0.004}/SiO_2$ is ascribed to the geometric effect, as no electronic effect is observed. An unexpected result is that the selectivity of $NiZn_{0.07}/SiO_2$ is lower than that of Ni/SiO_2 although the number of active sites of the former is smaller than that of the latter. It seems that the presence of ZnO, with the opposite effect of Ni–Zn alloy, is responsible for the lower selectivity of $NiZn_{0.07}/SiO_2$.

For $NiCo_x/SiO_2$, the selectivity to styrene is ranked in the order $NiCo_{0.09}/SiO_2$ (88.0%) > $NiCo_{0.52}/SiO_2$ (69.5%) > Ni/SiO_2 (64.4%) > $NiCo_{1.02}/SiO_2$ (56.4%) > Co/SiO_2 (55.4%) > $NiCo_{1.97}/SiO_2$ (43.1%) (Fig. 3d). Interestingly, $NiCo_{0.09}/SiO_2$ without Ni–Co alloy has the highest selectivity, while other $NiCo_x/SiO_2$ (x = 0.52, 1.02, and 1.97) show a selectivity of below 70%. The low selectivity of $NiCo_x/SiO_2$ (x = 0.52, 1.02, and 1.97) is a consequence of further hydrogenation of styrene induced by a strong adsorption of styrene, in view of the electron-poor nature of Ni active sites on these catalysts. By contrast, because there is only a geometric effect but no electronic effect between Ni and Co on $NiCo_{0.09}/SiO_2$, this catalyst shows a high selectivity to styrene. It is observed that the selectivity of $NiCo_{0.52}/SiO_2$ is slightly higher than that of Ni/SiO_2, which is likely due to a trade-off between the electronic effect and the geometric effect.

It can be seen from the above results that among all the catalysts studied here, $NiCo_{0.09}/SiO_2$ exhibits the highest selectivity to styrene at complete conversion of phenylacetylene. When compared to non-precious metal catalysts in the literature, the selectivity of $NiCo_{0.09}/SiO_2$ remains at a high level. As presented in Table 2, under the premise of > 99% conversion of phenylacetylene, only four catalysts, i.e., $NiZn_3$/AlSBA-15(40) [24], $NiZn_3/Al_2O_3$ [25], $Ni_3Sn/MgAl_2O_4$ [28], and 450-$NiSi_x$ [61], show higher selectivity to styrene than $NiCo_{0.09}/SiO_2$. However, $Ni_3Sn/MgAl_2O_4$ [28] and 450-$NiSi_x$ [61] are tested under a phenylacetylene/Ni molar ratio (49 and 6) much lower than that for $NiCo_{0.09}/SiO_2$ (361), meaning that much more Ni is required. For $NiZn_3$/AlSBA-15(40) [24], the complicated preparation method and expensive reagents limit its practical application. It should be noted that the above comparison is rather crude because the reaction conditions (e.g., temperature, pressure, solvent and time) vary with each study.

In addition, $NiCo_{0.09}/SiO_2$ is comparable to the commercial Lindlar catalyst (Pd–Pb/$CaCO_3$ with a Pd loading of 5 wt%, manufactured by Aladdin Reagent Int. (Shanghai, China)) in terms of selectivity. Under the same condition, the Lindlar catalyst can achieve a conversion of 99.5% and a selectivity of 88.7% at 640 min of reaction [25]. Although the apparent activity of $NiCo_{0.09}/SiO_2$ (910 min of reaction) is somewhat smaller than that of the Lindlar catalyst, $NiCo_{0.09}/SiO_2$ is substantially more cost effective from the economic point of view, and thus an attractive alternative to the Lindlar catalyst.

Reusability of $NiCo_{0.09}/SiO_2$

Six consecutive cycles were performed, with the reaction time fixed at 910 min for each cycle. The magnetic $NiCo_{0.09}/SiO_2$ can be easily recycled from the solution

Table 2 Performance comparison of non-precious metal catalysts in selective hydrogenation of phenylacetylene

Catalyst	Solvent	S/C[a]	T (°C)	P (MPa)	Time (min)	Conv. (%)	Sel. (%)	Refs.
$NiZn_3$/AlSBA-15(40)	Methanol	1064	40	0.1	930	99.6	90.3	[24]
$NiZn_3/Al_2O_3$	Methanol	833	60	0.5	850	> 99	92	[25]
pre-NiCu/MMO	2-propanol	61	100	0.4	180	95.8	90.3	[26]
$Ni_5Mg_4Ga_3$-500	2-propanol	15	40	0.3	300	95.1	92.2	[27]
$Ni_3Sn/MgAl_2O_4$	Hexane	~49	40	0.5	1200	> 99	89	[28]
350–450-$NiSi_x$	Ethanol	~4	50	0.4	300	97	88	[29]
Ni_2Si/SiO_2	Ethanol	~9	80	1.0	240	79.0	87.7	[30]
Ni_2Si-450/SBA-15	Ethanol	~3	40	1.0	210	> 99	~77	[31]
Ni_2P/Al_2O_3	2-propanol	16.5	100	0.3	180	98.6	88.2	[32]
Ni_2P/MZSM-5-2	Ethanol	~90	100	1.0	105	~99	~85	[33]
Co/Phen@SiO_2-800	Acetonitrile	25	90	4.0	480	93	94.6	[39]
Ni-fructose@SiO_2-800	Acetonitrile	153	110	1.0	300	–	88[b]	[41]
450-$NiSi_x$	Ethanol	~6	50	0.4	180	~99	~91	[61]
Ni_2P	Dioxane	7.5	85	0.6	360	98	96	[63]
Ni-CNFs(1)/MS	2-propanol	~58	80	0.1	180	90.8	~90	[64]
Ni NSs	Ethanol	~3	50	0.1	1200	98	89	[65]
H_{350}-Ni/COF	Methanol	147	100	1.0	60	> 99	85	[66]
$NiCo_{0.09}/SiO_2$	Ethanol	361	60	0.5	910	99.5	88	this work

[a]Phenylacetylene/Ni(or Co) molar ratio

[b]Yield of styrene

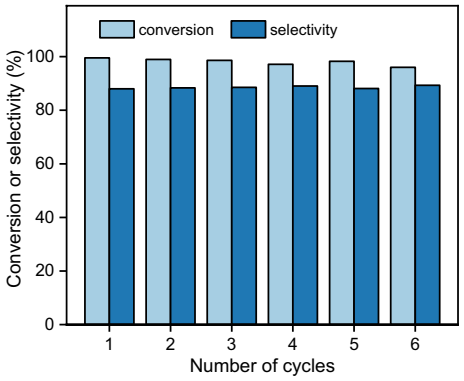

Fig. 4 Reusability of $NiCo_{0.09}/SiO_2$ in 6 consecutive cycles of reaction (reaction condition: 60 °C, 0.5 MPa, 5 wt% phenylacetylene in ethanol, 0.15 g of catalyst, and 100 g of solution in a semi-batch stirred tank reactor)

by magnetic separation. As shown in Fig. 4, the selectivity to styrene is maintained at 88% during 6 cycles, while the conversion of phenylacetylene decreases slightly from 99.5 to 96.0%, which may be related to the mass loss of the catalyst during the recycling process. The metal particles of the used $NiCo_{0.09}/SiO_2$ remain uniformly

dispersed on SiO_2 with an average particle size of 4.3 nm (Fig. S9), similar to that of the fresh catalyst (4.1 nm). Additionally, ICP-OES analysis shows that the loadings of Ni and Co in the used $NiCo_{0.09}/SiO_2$ are 5.1 and 0.5 wt%, respectively, which are almost the same as those of the fresh catalyst (5.3 and 0.5 wt% for Ni and Co), indicating no metal leaching during the cyclic operation. These results demonstrate that $NiCo_{0.09}/SiO_2$ has good stability in the selective hydrogenation of phenylacetylene.

Effect of reaction conditions

Finally, the effects of reaction temperature and pressure on the activity and selectivity of phenylacetylene hydrogenation over $NiCo_{0.09}/SiO_2$ are examined (Fig. S10). The reaction temperature and pressure range from 50 to 80 °C and from 0.3 to 0.9 MPa, which are determined based on industrial data [67]. When the pressure is constant at 0.5 MPa, the reaction time for complete conversion of phenylacetylene is shortened from 1140 to 450 min with increasing the reaction temperature from 50 to 80 °C, while the selectivity to styrene decreases from 89.1 to 82.7%. On the other hand, when the temperature is constant at 60 °C, the reaction time for complete conversion of phenylacetylene reduces from 1040 to 600 min as the pressure varies from 0.3 to 0.9 MPa, corresponding to a drop in the selectivity from 88.3 to 83.0%. It is clearly shown that an increase in temperature or pressure is beneficial for enhancing the apparent rate of phenylacetylene hydrogenation, but unfavorable for the selectivity to styrene. Therefore, a compromise is necessary in determining an acceptable reaction rate that would provide a good selectivity to styrene. However, this issue belongs to the optimization problem, which is beyond the scope of this paper.

Conclusions

A series of $NiZn_x/SiO_2$ and $NiCo_x/SiO_2$ bimetallic catalysts were prepared by pyrolysis of glucose and applied to selective hydrogenation of phenylacetylene. CO chemisorption, XRD, HRTEM, and XPS analyses revealed that the Ni–Zn alloy was formed in $NiZn_{0.02}/SiO_2$ and $NiZn_{0.05}/SiO_2$, while the Ni–Co alloy was formed in $NiCo_{0.52}/SiO_2$, $NiCo_{1.02}/SiO_2$, and $NiCo_{1.97}/SiO_2$. In addition, XPS and DRIFTS measurements showed the electron transfer from Zn to Ni for Ni–Zn bimetallic catalysts and from Ni to Co for Ni–Co catalysts. The performance of bimetallic catalysts in the selective hydrogenation of phenylacetylene strongly depended on the Zn/Ni and Co/Ni molar ratios. Compared to monometallic Ni/SiO_2, $NiZn_{0.05}/SiO_2$ and $NiCo_{0.09}/SiO_2$ exhibited reduced apparent activity but significantly enhanced styrene selectivity of 86.3% and 88.0%, at above 99% conversion of phenylacetylene. For $NiZn_{0.05}/SiO_2$, the enhancement in the selectivity was due to the geometric and electronic effects induced by Ni–Zn alloy, while for $NiCo_{0.09}/SiO_2$, it was mainly attributed to the geometric effect caused by Co doping. $NiCo_{0.09}/SiO_2$ was proven to be recyclable for 6 cycles almost without structural and performance changes.

Therefore, non-precious $NiCo_{0.09}/SiO_2$ is a promising catalyst for the selective hydrogenation of phenylacetylene.

Supplementary information

The online version contains supplementary material available.

Supplementary Information The online version contains supplementary material available at https://doi.org/10.1007/s11144-022-02276-w.

Acknowledgements This work was financially supported by the National Natural Science Foundation of China (Grant No. 21978093).

Declarations

Conflict of interest The authors declare that they have no conflict of interest.

References

1. Maul J, Frushour BG, Kontoff JR, Eichenauer H, Ott K-H, Schade C (2007) In: Ley C (ed) Ullmann's encyclopedia of industrial chemistry. Wiley-VCH, Weinheim
2. Maximize Market Research (2021) Styrene market: global market forecast and growth opportunities by 2027. https://www.maximizemarketresearch.com/market-report/global-styrene-market/23532/. Accessed 10 May 2022
3. Ghasemzadeh K, Zeynali R, Bahadori F, Basile A (2018) CFD analysis of Pd-Ag membrane reactor performance during ethylbenzene dehydrogenation process. Int J Hydrog Energy 43:7675–7683
4. Pérez Valencia JP, San Nicolás Sayans E (2011) Styrene production through 1-phenylethanol vapor-phase dehydration in a new reaction system. Ind Eng Chem Res 50:5485–5489
5. Lee F-M, Gentry JC, Wytcherley RW (1998) Recovery of styrene from pyrolysis gasoline by extractive distillation. US Patent 5849982
6. Zhou Z, Hu J, Zhang R, Li L, Cheng Z (2015) Revisiting the reaction kinetics of selective hydrogenation of phenylacetylene over an egg-shell catalyst in excess styrene. Chem Eng Sci 138:663–672
7. Pang M, Shao Z, Wang X, Liang C, Xia W (2015) Toward economical purification of styrene monomers: eggshell Mo_2C for front-end hydrogenation of phenylacetylene. AlChE J 61:2522–2531
8. Delgado JA, Benkirane O, Claver C, Curulla-Ferre D, Godard C (2017) Advances in the preparation of highly selective nanocatalysts for the semi-hydrogenation of alkynes using colloidal approaches. Dalton Trans 46:12381–12403
9. Zhang L, Zhou M, Wang A, Zhang T (2020) Selective hydrogenation over supported metal catalysts: from nanoparticles to single atoms. Chem Rev 120:683–733
10. Weerachawanasak P, Mekasuwandumrong O, Arai M, Fujita S-I, Praserthdam P, Panpranot J (2009) Effect of strong metal-support interaction on the catalytic performance of Pd/TiO_2 in the liquid-phase semihydrogenation of phenylacetylene. J Catal 262:199–205
11. Hu J, Zhou Z, Zhang R, Li L, Cheng Z (2014) Selective hydrogenation of phenylacetylene over a nano-Pd/α-Al_2O_3 catalyst. J Mol Catal A 381:61–69
12. Yang L, Jin Y, Fang X, Cheng Z, Zhou Z (2017) Magnetically recyclable core-shell structured Pd-based catalysts for semihydrogenation of phenylacetylene. Ind Eng Chem Res 56:14182–14191
13. Markov PV, Mashkovsky IS, Bragina GO, Wärnå J, Gerasimov EY, Bukhtiyarov VI, Stakheev AY, Murzin DY (2019) Particle size effect in liquid-phase hydrogenation of phenylacetylene over Pd catalysts: experimental data and theoretical analysis. Chem Eng J 358:520–530
14. Boucher MB, Zugic B, Cladaras G, Kammert J, Marcinkowski MD, Lawton TJ, Sykes ECH, Flytzani-Stephanopoulos M (2013) Single atom alloy surface analogs in $Pd_{0.18}Cu_{15}$ nanoparticles for selective hydrogenation reactions. Phys Chem Chem Phys 15:12187–12196

15. Wang Z, Yang L, Zhang R, Li L, Cheng Z, Zhou Z (2016) Selective hydrogenation of phenylacetylene over bimetallic Pd-Cu/Al_2O_3 and Pd-Zn/Al_2O_3 catalysts. Catal Today 264:37–43
16. Li Z, Hu M, Liu B, Liu J, Wang P, Yao J, Zhang X, He M, Song W (2021) Pd-Zn alloy nanoparticles encapsulated into mesoporous silica with confinement effect for highly selective semi-hydrogenation of phenylacetylene. ChemCatChem 13:868–873
17. Zhang J, Xu W, Xu L, Shao Q, Huang X (2018) Concavity tuning of intermetallic Pd-Pb nanocubes for selective semihydrogenation catalysis. Chem Mater 30:6338–6345
18. Wang L, Yin P, Zhang L-L, Shen S-C, Xu S-L, Chen P, Liang H-W (2020) Nitrogen-fixing of ultrasmall Pd-based bimetallic nanoclusters on carbon supports. J Catal 389:297–304
19. Xiang L, Feng H, Liu M, Zhang X, Fan G, Li F (2021) Surface defect-induced site-specific dispersion of Pd nanoclusters on TiO_2 nanoparticles for semihydrogenation of phenyl acetylene. ACS Appl Nano Mater 4:4688–4698
20. Tian H, Huang F, Zhu Y, Liu S, Han Y, Jaroniec M, Yang Q, Liu H, Lu GQM, Liu J (2018) The development of yolk-shell-structured Pd&ZnO@Carbon submicroreactors with high selectivity and stability. Adv Funct Mater 28:1801737
21. Choe K, Zheng F, Wang H, Yuan Y, Zhao W, Xue G, Qiu X, Ri M, Shi X, Wang Y, Li G, Tang Z (2020) Fast and selective semihydrogenation of alkynes by palladium nanoparticles sandwiched in metal-organic frameworks. Angew Chem Int Ed 59:3650–3657
22. Huang F, Jia Z, Diao J, Yuan H, Su D, Liu H (2019) Palladium nanoclusters immobilized on defective nanodiamond-graphene core-shell supports for semihydrogenation of phenylacetylene. J Energy Chem 33:31–36
23. Cherkasov N, Murzin DY, Catlow CRA, Chutia A (2021) Selectivity of the Lindlar catalyst in alkyne semi-hydrogenation: a direct liquid-phase adsorption study. Catal Sci Technol 11:6205–6216
24. Yang L, Yu S, Peng C, Fang X, Cheng Z, Zhou Z (2019) Semihydrogenation of phenylacetylene over nonprecious Ni-based catalysts supported on AlSBA-15. J Catal 370:310–320
25. Bao Z, Yang L, Cheng Z, Zhou Z (2020) Selective hydrogenation of the C_8 aromatic fraction of pyrolysis gasoline over $NiZn_3$/α-Al_2O_3: experimental and modeling studies. Ind Eng Chem Res 59:4322–4332
26. Liu Y, Zhao J, Feng J, He Y, Du Y, Li D (2018) Layered double hydroxide-derived Ni-Cu nanoalloy catalysts for semi-hydrogenation of alkynes: improvement of selectivity and anti-coking ability via alloying of Ni and Cu. J Catal 359:251–260
27. Li C, Chen Y, Zhang S, Zhou J, Wang F, He S, Wei M, Evans DG, Duan X (2014) Nickel-gallium intermetallic nanocrystal catalysts in the semihydrogenation of phenylacetylene. ChemCatChem 6:824–831
28. Liu Y, Liu X, Feng Q, He D, Zhang L, Lian C, Shen R, Zhao G, Ji Y, Wang D, Zhou G, Li Y (2016) Intermetallic Ni_xM_y (M = Ga and Sn) nanocrystals: a non-precious metal catalyst for semi-hydrogenation of alkynes. Adv Mater 28:4747–4754
29. Chen X, Zhao A, Shao Z, Li C, Williams CT, Liang C (2010) Synthesis and catalytic properties for phenylacetylene hydrogenation of silicide modified nickel catalysts. J Phys Chem C 114:16525–16533
30. Yang K, Chen X, Guan J, Liang C (2015) Nickel silicides prepared from organometallic polymer as efficient catalyst towards hydrogenation of phenylacetylene. Catal Today 246:176–183
31. Yang K, Chen X, Wang L, Zhang L, Jin S, Liang C (2017) SBA-15-supported metal silicides prepared by chemical vapor deposition as efficient catalysts towards the semihydrogenation of phenylacetylene. ChemCatChem 9:1337–1342
32. Chen Y, Li C, Zhou J, Zhang S, Rao D, He S, Wei M, Evans DG, Duan X (2015) Metal phosphides derived from hydrotalcite precursors toward the selective hydrogenation of phenylacetylene. ACS Catal 5:5756–5765
33. Fu W, Zhang L, Tao T, Tang T (2021) Highly dispersed Ni_2P clusters inlaid in micropore openings on mesoporous ZSM-5 zeolite and its catalytic performance in the phenylacetylene semi-hydrogenation. J Ind Eng Chem 95:376–387
34. Furukawa S, Ozawa K, Komatsu T (2013) Preparation of alumina-supported intermetallic compounds. RSC Adv 3:23269–23277
35. Furukawa S, Komatsu T (2017) Intermetallic compounds: promising inorganic materials for well-structured and electronically modified reaction environments for efficient catalysis. ACS Catal 7:735–765

36. Jagadeesh Rajenahally V, Surkus A-E, Junge H, Pohl M-M, Radnik J, Rabeah J, Huan H, Schünemann V, Brückner A, Beller M (2013) Nanoscale Fe_2O_3-based catalysts for selective hydrogenation of nitroarenes to anilines. Science 342:1073–1076
37. Westerhaus FA, Jagadeesh RV, Wienhöfer G, Pohl M-M, Radnik J, Surkus A-E, Rabeah J, Junge K, Junge H, Nielsen M, Brückner A, Beller M (2013) Heterogenized cobalt oxide catalysts for nitroarene reduction by pyrolysis of molecularly defined complexes. Nat Chem 5:537–543
38. Pisiewicz S, Formenti D, Surkus A-E, Pohl M-M, Radnik J, Junge K, Topf C, Bachmann S, Scalone M, Beller M (2016) Synthesis of nickel nanoparticles with N-doped graphene shells for catalytic reduction reactions. ChemCatChem 8:129–134
39. Chen F, Kreyenschulte C, Radnik J, Lund H, Surkus A-E, Junge K, Beller M (2017) Selective semihydrogenation of alkynes with N-graphitic-modified cobalt nanoparticles supported on silica. ACS Catal 7:1526–1532
40. Ryabchuk P, Agostini G, Pohl M-M, Lund H, Agapova A, Junge H, Junge K, Beller M (2018) Intermetallic nickel silicide nanocatalyst-A non-noble metal-based general hydrogenation catalyst. Sci Adv 4:eaat0761
41. Murugesan K, Alshammari AS, Sohail M, Beller M, Jagadeesh RV (2019) Monodisperse nickel-nanoparticles for stereo- and chemoselective hydrogenation of alkynes to alkenes. J Catal 370:372–377
42. Abd-Elrahman MI, Ahmed SM (2009) Thermal degradation kinetics and geometrical stability of D-sucrose. Int J Polym Mater Polym Biomater 58:322–335
43. Cheng F, Dupont V, Twigg MV (2016) Temperature-programmed reduction of nickel steam reforming catalyst with glucose. Appl Catal A 527:1–8
44. Dai X, Chen Z, Yao T, Zheng L, Lin Y, Liu W, Ju H, Zhu J, Hong X, Wei S, Wu Y, Li Y (2017) Single Ni sites distributed on N-doped carbon for selective hydrogenation of acetylene. Chem Commun 53:11568–11571
45. Montie MG, Santiago-Jacinto P, Góngora JAID, Reguera E, Rodríguez-Gattorno G (2011) Synthesis and thermal behavior of metallic cobalt micro and nanostructures. Nano-Micro Lett 3:12–19
46. Spanjers CS, Sim RS, Sturgis NP, Kabius B, Rioux RM (2015) In situ spectroscopic characterization of $Ni_{1-x}Zn_x$/ZnO catalysts and their selectivity for acetylene semihydrogenation in excess ethylene. ACS Catal 5:3304–3315
47. Meng X, Wang L, Chen L, Xu M, Liu N, Zhang J, Yang Y, Wei M (2020) Charge-separated metal-couple-site in NiZn alloy catalysts towards furfural hydrodeoxygenation reaction. J Catal 392:69–79
48. Wang Z, Wang C, Chen S, Liu Y (2014) Co-Ni bimetal catalyst supported on perovskite-type oxide for steam reforming of ethanol to produce hydrogen. Int J Hydrog Energy 39:5644–5652
49. Gao X, Tan Z, Hidajat K, Kawi S (2017) Highly reactive Ni-Co/SiO_2 bimetallic catalyst via complexation with oleylamine/oleic acid organic pair for dry reforming of methane. Catal Today 281:250–258
50. Thommes M, Kaneko K, Neimark AV, Olivier JP, Rodriguez-Reinoso F, Rouquerol J, Sing KSW (2015) Physisorption of gases, with special reference to the evaluation of surface area and pore size distribution (IUPAC Technical Report). Pure Appl Chem 87:1051–1069
51. Yang J, Shen X, Zhu G, Ji Z, Zhou H (2014) ZnNi alloy nanoparticles grown on reduced graphene oxide nanosheets and their magnetic and catalytic properties. RSC Adv 4:386–394
52. Xin J, Cui H, Cheng Z, Zhou Z (2018) Bimetallic Ni-Co/SBA-15 catalysts prepared by urea coprecipitation for dry reforming of methane. Appl Catal A 554:95–104
53. Wang Y, Liu B, Lan X, Wang T (2021) Subsurface carbon as a selectivity promotor to enhance catalytic performance in acetylene semihydrogenation. ACS Catal 11:10257–10266
54. Yue X, Zhang L, Sun L, Gao S, Gao W, Cheng X, Shang N, Gao Y, Wang C (2021) Highly efficient hydrodeoxygenation of lignin-derivatives over Ni-based catalyst. Appl Catal B 293:120243
55. Wu H, Liu H, Yang W, He D (2016) Synergetic effect of Ni and Co in Ni-Co/SBA-15-CD catalysts and their catalytic performance in carbon dioxide reforming of methane to syngas. Catal Sci Technol 6:5631–5646
56. Agnelli M, Swaan HM, Marquez-Alvarez C, Martin GA, Mirodatos C (1998) CO hydrogenation on a nickel catalyst: II. A mechanistic study by transient kinetics and infrared spectroscopy. J Catal 175:117–128
57. Layman KA, Bussell ME (2004) Infrared spectroscopic investigation of CO adsorption on silica-supported nickel phosphide catalysts. J Phys Chem B 108:10930–10941

58. Arpini BH, Braga AH, Borges LR, Vidinha P, Gonçalves RV, Szanyi J, Rossi LM (2022) Tuning CO_2 hydrogenation selectivity by N-doped carbon coating over nickel nanoparticles supported on SiO_2. ACS Sustain Chem Eng 10:2331–2342
59. Smith ML, Kumar N, Spivey JJ (2012) CO adsorption behavior of Cu/SiO_2, Co/SiO_2, and CuCo/SiO_2 catalysts studied by in situ DRIFTS. J Phys Chem C 116:7931–7939
60. Ma R, Yang T, Sun J, He Y, Feng J, Miller JT, Li D (2019) Nanoscale surface engineering of PdCo/Al_2O_3 catalyst via segregation for efficient purification of ethene feedstock. Chem Eng Sci 210:115216
61. Chen X, Li M, Guan J, Wang X, Williams CT, Liang C (2012) Nickel-silicon intermetallics with enhanced selectivity in hydrogenation reactions of cinnamaldehyde and phenylacetylene. Ind Eng Chem Res 51:3604–3611
62. Kong X, Zhu Y, Zheng H, Zhu Y, Fang Z (2017) Inclusion of Zn into metallic Ni enables selective and effective synthesis of 2,5-dimethylfuran from bioderived 5-hydroxymethylfurfural. ACS Sustain Chem Eng 5:11280–11289
63. Carenco S, Leyva-Pérez A, Concepción P, Boissière C, Mézailles N, Sanchez C, Corma A (2012) Nickel phosphide nanocatalysts for the chemoselective hydrogenation of alkynes. Nano Today 7:21–28
64. Donphai W, Kamegawa T, Chareonpanich M, Yamashita H (2014) Reactivity of Ni–carbon nanofibers/mesocellular silica composite catalyst for phenylacetylene hydrogenation. Ind Eng Chem Res 53:10105–10111
65. Yu J-W, Wang X-Y, Yuan C-Y, Li W-Z, Wang Y-H, Zhang Y-W (2018) Synthesis of ultrathin Ni nanosheets for semihydrogenation of phenylacetylene to styrene under mild conditions. Nanoscale 10:6936–6944
66. Wang N, Liu J, Zhang M, Wang C, Li X, Ma L (2021) Non-noble nickel-modified covalent organic framework for partial hydrogenation of aromatic terminal alkynes. ACS Appl Mater Interfaces 13:60135–60143
67. Li S, Liu J, Zhu Z, Zhu J, Kuai J (2014) Method for selective hydrogenation of phenylacetylene using composite bed in the presence of styrene. US Patent 8916736